Bigger makes surprisingly better: coarse RuP crystallines for hydrogen evolution reaction truly beating benchmark Pt nanocatalysts

Jie Yu, Yanan Guo, Sixuan She, Shuanshuan Miao, Meng Ni, Wei Zhou*, Meilin Liu, and Zongping Shao*

J. Yu, Prof. Y.N. Guo, S.X. She, S.S. Miao, Prof. W. Zhou, Prof. Z.P. Shao
State Key Laboratory of Materials-Oriented Chemical Engineering, College of Chemical Engineering, Nanjing Tech University, No. 5, Xin Mofan Road, Nanjing 210009, PR China
Tel.: +86 2583172256; fax: +86 25 83172242
E-mail: zhouwei1982@njtech.edu.cn (W. Zhou) shaozp@njtech.edu.cn (Z.P. Shao)

Prof. M. Ni
Building Energy Research Group, Department of Building and Real Estate, The Hong Kong Polytechnic University, Hung Hom, Kowloon, 999077, Hong Kong, China

Prof. M.L. Liu
Center for Innovative Fuel Cell and Battery Technologies, School of Materials Science and Engineering, Georgia Institute of Technology, Atlanta, Georgia 30332-0245, United States

Prof Z.P. Shao
Department of Chemical Engineering, Curtin University, Perth, Western Australia 6845, Australia

Abstract

Although metallic ruthenium (Ru) is a potential hydrogen evolution reaction (HER) electrocatalyst to replace platinum (Pt) at a price only ~4% of Pt, the robust dissolution of Ru under operation conditions remains a big challenge. Here, we demonstrate a coarse-type ruthenium phosphide (L-RP) performs surprisingly more active and stable than metallic Ru nanoparticles and nanosized RuP counterpart (S-RP, 1-3 nm). In particular, L-RP/C achieves an HER performance surpassing Pt/C at a wide pH range from almost all aspects, reflected by lower overpotential at a current density of 10 mA cm^{-2}, lower Tafel slope, higher exchange current density, larger turnover frequency, and 200 h stable operation. Calculation reveals that the Gibbs free energy of hydrogen adsorption (ΔG_{H^*}) of RuP is much closer to zero than that of metallic Ru catalyst and phosphorous doping is proved to enhance the proton-transfer in HER, contributing in part to the improved activity of RuP. The better activity and stability of L-RP relative to S-RP is ascribed to the stabilization of P species due to the lowered surface energy

of large particles. The relatively low price of raw material, facile synthesis, super-high activity in a wide pH range and favorable stability make the L-RP/C a highly attractive next-generation HER electrocatalyst for efficient water electrolysis with great application potential.

Hydrogen is one of the most environmentally benign and renewable alternatives to the conservative fossil fuels[1-3]. A further combination of hydrogen energy and fuel cell technology may provide an ideal energy system solution for the future with high sustainability[4, 5]. As the most promising approach to generate high-purity hydrogen, water splitting will provide an endless supply of hydrogen fuel with zero carbon emission in nature[6, 7]. Water splitting involves both oxygen evolution reaction (OER) at the anode and hydrogen evolution reaction (HER) at the cathode of an electrolyzer. As the core for scalable hydrogen production from water electrolysis, the HER requires highly efficient electrocatalysts to achieve favorable reaction kinetics at the expanse of minimal overpotential[8, 9]. Platinum (Pt) nanoparticles supported on carbon substrates are the benchmark HER catalysts with high activity in a wide range of pH values of the electrolyte solutions, whereas its large-scale use in water electrolyzers is strictly limited by its formidable cost, scarcity and insufficient stability[10-12]. To realize the practical use of water splitting for hydrogen generation, it is highly desirable to explore alternative Pt-free HER catalysts with sufficiently high activity and stability.

To date, numerous potential earth-abundant material candidates have been exploited as HER electrocatalysts, mainly performing in acidic electrolytes[13-16]. In the promising photo-electrochemical water splitting technology, however, the best oxygen evolution reaction (OER) electrocatalysts used as counter electrodes work well only in basic or neutral media[15, 17]. Unfortunately, most of the available Pt-free catalysts still showed inferior performance than Pt/C in basic electrolyte[18-20]. It suggests further development in non-Pt electrocatalysts for HER with high activity and adequate stability at a wide pH range, especially under alkaline or neutral conditions, is urgently needed.

Attracted by its similar properties but much lower price to platinum (only ~4%), ruthenium (Ru) has received increasing attention as potential HER electrocatalysts[9, 15, 18, 21-23]. To achieve high activity for HER, the particle size of the as-prepared Ru catalysts is always in nanometer range to maximize the number of active sites. For example, anomalously structured Ru nanoparticles[15], two-dimensional Ru nanosheets[21], one-dimensional RuO_2 nanowires on g‑carbon nitride[22] have been developed, showing attractive performance for HER. Very recently, Mahmood et al. fabricated a Ru@C_2N hybrid (Ru nanoparticles dispersed within a nitrogenated holey two-dimensional carbon structure), which showed remarkably high electrocatalytic performance towards HER in both acid and alkaline soutions[18]. In addition, the RuCo@NC hybrid material developed by Su et al. also exhibited an amazing HER activity in 1 M KOH solution[9]. In particular, it's more worth emphasizing that metallic Ru is more active than RuO_2 for HER in identical experimental conditions. However, metallic Ru has the dissolution

rate in both acid and alkaline solutions several orders of magnitude higher compared to the ruthenium oxide, leading to its poor stability of nanosized Ru[23]. The high fabrication cost of nanostructured catalysts may be another concern for practical use. To realize practical use of Ru, it is thus crucial yet a big challenge to improve the operational stability while maintaining high activity.

In the present work, we report a coarse-type ruthenium phosphide (RuP), which can be facilely prepared with mass production capability, as an outstanding HER electrocatalyst in a wide range of pH values, beating the benchmark Pt/C nanocatalysts from all aspects, including price, activity and stability. Attractively, it shows low overpotentials of 18, 19, and 80 mV at 10 mA cm^{-2} in 1 M KOH, 0.5 M H_2SO_4 and 1 M PBS electrolytes, respectively, as well as superior stability for 200 h in solutions with a wide range of pH values, far more active and stable than the P-free Ru/C counterpart and outperforms all the reported catalysts. Fairly surprisingly, the coarse type nature of the catalyst (L-RP/C) results in 50 folds of improvement in intrinsic catalytic activity of RuP for HER as compared to nanosized RuP counterpart (S-RP/C). In addition, the coarse-type morphology structure ensures a significant cost reduction in catalyst preparation and improved stability. All above features make the coarse-type RuP as a highly promising HER electrocatalyst with substantial application potential in industrial scale water splitting systems.

Synthesis and characterization of the L-RP/C and S-RP/C catalysts

A schematic diagram illustrating the facile synthesis of the coarse-type RuP-based catalyst (L-RP/C) is depicted in Supplementary Fig. 1, which mainly involves low-temperature phosphorization of commercial ruthenium chloride ($RuCl_3$) precursor (which is denoted as L-RP) and subsequent mixing with carbon by hand grinding. Several RuP-carbon composites with different mass ratios of RuP and conductive carbon (which is labeled as L-RP/C-x, where x refers to the mass ratio of Ru) were prepared to optimize the HER activity with respect to 20% Pt/C (Supplementary Fig. 2), and the L-RP/C-0.2 is specifically denoted as L-RP/C. To demonstrate the advantageous features of coarse-type RuP for HER, nanosized RuP-based catalyst (S-RP/C) was also synthesized for comparative studies. For the preparation of S-RP/C, a certain amount of conductive carbon was first impregnated with proper amount of $RuCl_3$, and then a further phosphorization by NaH_2PO_2 in Ar atmosphere was conducted.

The formation of RuP crystalline phase in L-RP and S-RP/C was confirmed by the ex-situ X-ray diffraction (XRD) pattern (Fig. 1a). The diffraction peaks for the L-RP can be well indexed to orthorhombic RuP phase[24]. Except for the broad peaks at about 25 ° and 43 ° belonging to the conductive carbon, three weak peaks at 31.91 °, 44.02 ° and 46.02 ° were also observed for the S-RP/C, which are indexed to (011), (112) and (211) reflections of orthorhombic RuP, manifesting the formation of RuP in the S-RP/C hybrid. The poor peak intensity suggests the small particle size of RuP phase in S-RP/C. The coarse nature of RuP phase in L-RP was revealed by means of transmission electron

microscopy (TEM) and scanning electron microscopy (SEM) observation (Fig. 1b and the inset of Fig. 1b), which demonstrated larger particles in the size of micrometers aggregated from primary particles with the size of 10-30 nm. According to the SEM image in the inset of Fig. 1c, we only discover the large carbon particles in S-RP/C, while the TEM image (Fig. 1c) discloses the homogeneous distribution of 1-3 nm RuP nanoparticles on the surface of conductive carbon particles, suggesting that the conductive carbon performed as a useful support for mediating the growth and suppressing the aggregation of RuP. The Ru content in the S-RP/C sample is about 21.4 wt%, as determined from the thermogravimetric analysis (TGA) under air conditions (Supplementary Fig. 3).

Fig. 1d &e present high-resolution TEM (HRTEM) images of L-RP, in which lattice fringe with spaces of 0.206 nm were observed, consistent with the distance of (112) plane of the orthorhombic RuP phase. An amorphous thin layer of approximately 1-2 nm was also observed over the surface of L-RP, which may belong to the passivated oxide film due to exposure to the air as often observed for metal phosphide materials[25, 26]. The selected area electron diffraction (SAED) pattern also confirms the RuP crystalline phase in nature of the primary particles (Fig. 1f). The crystal structure of RuP in S-RP/C is also clearly visible from the HRTEM images (Fig. 1g and 1h) and the corresponding fast-Fourier transform (FFT) pattern (Fig. 1i).

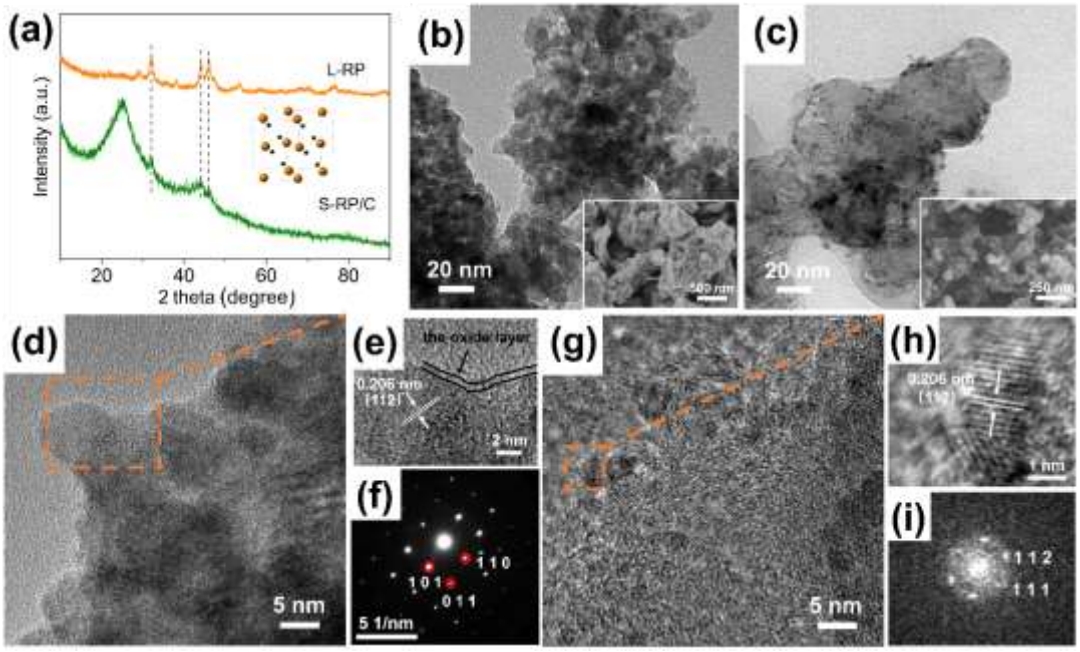

Figure 1 Morphology characterization and structural analysis of the L-RP and S-RP/C catalysts. (a) XRD patterns of as-synthesized L-RP and S-RP/C powders. The most obvious peaks represent the (011), (112) and (211) planes of RuP at approximately 31.91°, 44.02° and 46.02°. The insert of Fig. 2a shows the structure model of RuP. (b) The TEM image of L-RP with the particles of 10-30 nm agglomerating into larger chunks. The insert of Fig. 2b is the SEM image of L-RP. (c) TEM image of S-RP/C, showing the homogeneous distribution of 1-3 nm RuP nanoparticles on the surface of conductive carbon particles. The insert of Fig. 2c is the SEM image of S-RP/C. (d, e) HRTEM images and (f) an SAED pattern of L-RP. (g, h) HRTEM images and (i) the corresponding

FFT pattern of S-RP/C.

X-ray photoelectron spectroscopy (XPS) and energy dispersive X-ray (EDX) analysis were employed to study the composition and chemical state of the catalyst surface. XPS survey spectra confirms the presence of Ru, P, and O elements in both L-RP and S-RP/C samples (See survey scan spectrum, Supplementary Fig. 4). For the L-RP, Ru 3p3/2 and 3p1/2 core level peaks were observed at binding energies (BE) of 462.2 and 484.4 eV (Fig. 2a), together with Ru 3d5/2 and 3d3/2 subpeaks of RuP at 280.5 eV and 284.6 eV (Supplementary Fig. 5). The Ru 3p and 3d core level spectrum of the S-RP/C hybrid is almost identical to that of the L-RP, with binding energies of Ru 3p3/2, 3p1/2, 3d5/2 and 3d3/2 peaks at 462.2, 484.4, 280.5 and 284.6 eV, respectively (Fig. 2a and Supplementary Fig. 5), expect the C 1s peaks which are coexisted in Ru 3d region. These identical peak positions further verify the formation of RuP crystalline phase in the S-RP/C hybrid. Fig. 2b displays that the P 2p core level spectrum of L-RP has two peak regions with one at 130 and 130.9 eV (P 2p3/2 and 2p1/2) characteristic of phosphide signal, and the other assigned to phosphate-like P (P-O species) at 133.9 eV[27]. The strong peak associating with phosphate-like P could be ascribed to surface oxidation under ambient conditions, in line with the HRTEM analysis. The S-RP/C hybrid has the similar P 2p peak regions with L-RP, whereas the obviously improved intensity of phosphate signal /phosphide signal may result from more P reacting with the abundant oxygen species on the surface of pure carbon and P doped into carbon skeleton (P-O/P-C). Besides, the bulk Ru/P ratio measured by Energy-dispersive X-ray spectrum (EDX) was approximately 1:1 (Fig. 2c), agreeing well with the RuP phase as determined by the XRD and HRTEM characterizations discussed above. High-angle annular dark-field Scanning TEM (HAADF- STEM)-EDX line scan and mapping analysis (Fig. 2d-f) revealed uniform spatial distribution of Ru and P over the marked detection range of the constructed hybrid material. On the basis of N_2 adsorption/desorption isotherms, the Brunauer-Emmett-Teller (BET) specific surface areas of the L-RP, L-RP/C and S-RP/C were calculated to be 4.6, 37 and 28 $m^2 g^{-1}$ (Supplementary Fig. 6a-c), respectively. All BET results are also listed in Supplementary Table 1. The small specific surface area of L-RP is in well agreement with the coarse type of RuP particles. The larger specific surface area of L-RP/C than S-RP/C implies the impregnation/phosphorization processes caused the sintering of carbon support to some extent.

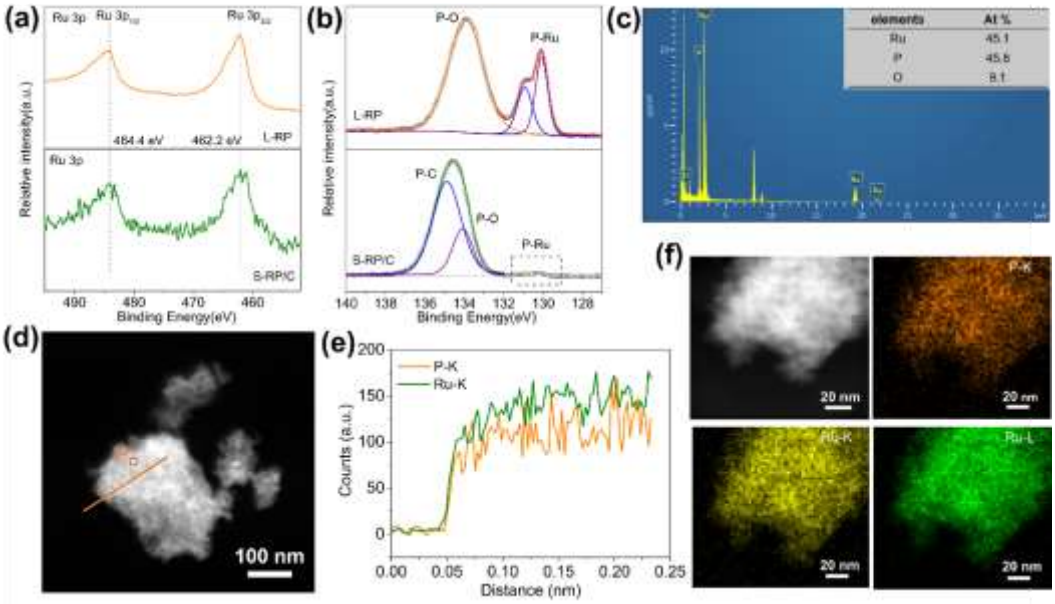

Figure 2 Structural characterization of the L-RP and S-RP/C catalysts. (a, b) High-resolution Ru 3p and P 2p XPS spectra of the as-prepared L-RP and S-RP/C. (c) EDX spectrum of L-RP measured at position P in Fig. 3d. (d) HAADF-STEM image of L-RP with orange line showing the line scanning path, and (e) the corresponding line-scanning profile. (f) HAADF-STEM image of L-RP and the corresponding element mapping images, displaying the uniform distribution of P (orange) and Ru (yellow, green).

Catalytic hydrogen evolution

The HER electrocatalytic activities of the L-RP/C, S-RP/C and carbon were firstly comparatively assessed in an Ar-saturated 1 M KOH electrolyte. As revealed in Fig. 3a, the pure carbon demonstrated a minimal background activity for H_2 evolution. On the contrary, both L-RP/C and S-RP/C electrocatalysts exhibited excellent HER activities. Specifically, the L-RP/C catalyst yielded a current density of 10 mA cm^{-2} at an overpotential of 18 mV (η_{10} = 18 mV), and the S-RP/C catalyst yielded a current density of 10 $mAcm^{-2}$ even at a slightly lower overpotential of 17 mV, superior to the commercial Pt/C (η_{10} = 25 mV) in Fig. 3c. The better HER activity of S-RP/C than L-RP/C should attribute to the exposure of more active sites and a higher charge-transfer rate of S-RP/C, reflected by the electrochemically active surface area (ECSA) and electrochemical impedance spectroscopy (EIS) (Supplementary Fig. 7). Meanwhile, the nearly overlapped polarization curves of L-RP/C and L-RP/PC (the carbon treated by NaH_2PO_2) rule out the positive effect of P doping into C on the HER activity (Supplementary Fig. 8). However, as an important figure of merit employed to evaluate the intrinsic electrocatalytic activity of a catalyst, the turnover frequency (TOF) of L-RP/C was turned out to be more than 50 times that of S-RP/C at η_{10} = 20 mV in basic media (Fig. 3b), revealing the higher intrinsic electrocatalytic activity of L-RP/C

(details of the calculation are provided in the Supplementary Note 1). What's more, the L-RP/C and S-RP/C electrocatalysts also performed well in neutral and acidic media, with Pt-like activity or even outperforming the Pt/C (Supplementary Fig. 9). However, the stability of S-RP/C severely hindered its development as an outstanding HER catalyst, which was discussed later.

Once more, we carried out a detailed evaluation of the electrocatalytic performance and the reaction kinetics of L-RP/C in all pH conditions (1 M KOH, 0.5 M H_2SO_4, and 1 M PBS,). As a comparison, the electrocatalytic activities of other typical nanocatalysts including 20% Ru/C and commercial 20% Pt/C catalysts were also investigated under the identical operation conditions. As displayed in Fig. 3c and Supplementary Fig. 10, L-RP/C shows the smallest overpotential of 18 mV at the current density of 10 mA cm^{-2} in a 1 M KOH electrolyte, even 7 mV less than Pt/C (25 mV), while that of Ru/C is 139 mV; in acidic and neutral media, it only took L-RP/C a low overpotential of 19 mV and 95 mV, respectively, to achieve a current density of 10 mA cm^{-2}, equal to or 15 mV higher than that of Pt/C (19 mV in acidic media and 80 mV in neutral media), while those for the Ru/C sample were much larger in both acidic and neutral electrolytes (150 mV in acidic media and 349 mV in neutral media). A lower Tafel slope is typically favorable for practical applications. In Fig. 3d, the resulting Tafel slope of 34 mV dec^{-1} for L-RP/C in base is lower than the value of Pt/C (35 mV dec^{-1}), presenting a Tafel-Volmer mechanism with electrochemical desorption of H_2 as the rate-determining step in the HER process. Meanwhile, a small value of Tafel slope 37 and 54 mV dec^{-1} was also observed in 0.5 M H_2SO_4 and 1 M PBS solution, respectively, which is a little higher than that of Pt/C (37 mV dec^{-1} in acidic media and 47 mV dec^{-1} mV in neutral media), and much lower than those of the Ru/C sample (Supplementary Fig. 11). The exchange current density (j_0) of the L-RP/C is obtained by extrapolation of the Tafel plots. In 1 M KOH, the value (3.07 mA cm^{-2}) is much larger than that of Ru/C (0.25 mA cm^{-2}) and even over 1.5 times that of the Pt/C (2.005 mA cm^{-2}), suggesting the more excellent intrinsic electrocatalytic activity of L-RP/C. To obtain a straightforward comparison, the corresponding η_{10} and j_0 of each catalyst in different media were listed by the histogram in Fig. 3e. All the results, i.e. η_{10}, the Tafel slope and j_0, manifest the outstanding performance of L-RP/C, which outperform all the reported HER catalysts, including both Pt-based and non-precious metals in the wide pH values (see Supplementary Table 2). After normalization by specific surface area, the L-RP/C catalyst still exhibits better HER activity than the Pt/C in the pH values of 0-14 (Supplementary Fig. 12). It is worth noting that Ru is economically advantageous with 266, 320 and 28 A per dollar generated at 50 mV overpotentials for L-RP/C in 1 M KOH, 0.5 M H_2SO_4 and 1 M PBS electrolytes, which are respectively about 4, 2.5 and 3 times more economic than utilizing the commercial Pt (Fig. 3f).

The turnover frequency (TOF) of the active site in L-RP/C, Ru/C and 20% Pt/C catalysts was also estimated based on the previously reported method (details of the calculation are provided in the Supplementary Note 1)[28, 29]. In particular, the TOFs of L-RP/C are 3.64 s^{-1}, 3.35 s^{-1} and 0.44 s^{-1} at a η_{10} value of 20 mV in the alkaline, acid and neutral solutions, respectively, surpassing that of 20% Pt/C (1.34 s^{-1}, 1.99 s^{-1} and

0.37 s^{-1} at η_{10} = 20 mV in the alkaline, acid and neutral solutions, respectively), and much larger than that obtained for the Ru/C catalyst in a wide pH range, as depicted in Fig. 3g and 3h, and Supplementary Fig. 13. The TOF values of other recently reported outstanding electrocatalysts in basic or acidic media, expect for the less reported neutral system, are listed in Fig. 3g and 3h[11, 15, 17, 28-33]. Clearly, the L-RP/C catalyst far exceeds them. Furthermore, it is reported that the larger electrochemical surface area (ECSA) provides richer catalytically active sites, may bringing about the enhanced activity. The increasing ECSA from L-RP/C to Ru/C (Supplementary Fig. 14) is an important contributor to the drastic increase in HER catalytic activity. The fast charge transfer is also reflected by the electrochemical impedance spectra (EIS). As expected, the L-RP/C composite catalyst exhibits much lower charge transfer resistance than the Ru/C (Supplementary Fig. 15), implying that the most efficient HER kinetics occurred at the interface of L-RP/C and the electrolyte.

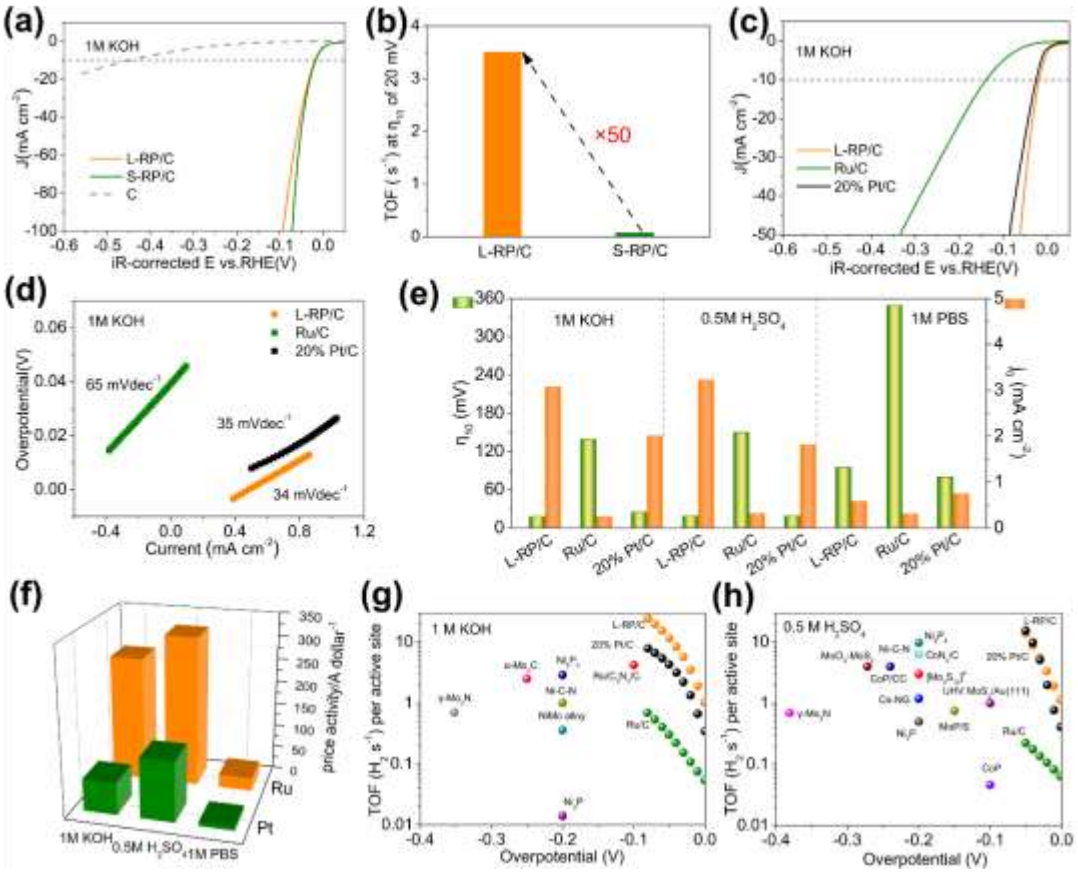

Figure 3 HER performance of different catalysts in a Ar-saturated solution. (a) HER polarization curves of L-RP/C, S-RP/C, and C catalysts loaded on the RDE (1600 rpm) in 1 M KOH solution. Scan rate, 5 mV s^{-1}. (b) Comparison of the TOF values of L-RP/C and S-RP/C. (c, d) HER polarization curves and the corresponding Tafel plots of L-RP/C, Ru/C, and 20% Pt/C catalysts loaded on the RDE (1600 rpm) in 1 M KOH solution. Scan rate, 5 mV s^{-1}. (e) Overpotentials at 10 mA cm^{-2} (left) and exchange current densities (right) of L-RP/C, Ru/C, and 20% Pt/C catalysts at a wide pH range. (f) Calculated price activities of L-RP/C and 20% Pt/C at a wide pH range. (g, h) TOF values of L-RP/C, Ru/C, and 20% Pt/C catalysts, with other recently reported HER

electrocatalysts in 1 M KOH (g) and 0.5 M H_2SO_4 (h) electrolytes.

Stability issues

Except for the activity, the operation stability of a catalyst is another crucial parameter for electrocatalysis. The operation stability of the Ru/C, L-RP/C and S-RP/C catalysts were then examined comparatively in a 1 M KOH electrolyte using a long-term cycling test. Unsurprisingly, the Ru/C showed the terrible durability in the basic solution (Fig. 4a), with tremendous degradation after only 1000 cyclic voltammetry (CV) cycles. This can be attributed to the dissolution of metallic Ru in the liquid electrolyte, as reported by Mayrhofer's group[23]. Nevertheless, after 5000 cyclic voltammetry (CV) cycles, the polarization curve of L-RP/C almost overlaps the curve of the initial test, just with the overpotential increased by 8 mV at a current density of 10 mA cm^{-2}, revealing the enhanced stability by incorporation of P into Ru. In striking contrast, the intrinsic instability of S-RP/C is exacerbated in spite of the excellent activity as a result of size control. The polarization curve of S-RP/C after only 1000 cyclic voltammetry (CV) cycles showed seriously negative shift by more than 96 mV at a current density of 10 mA cm^{-2} (Fig. 4a). The analogous results were obtained in neutral and acidic media (Supplementary Fig. 16). This leads S-RP/C to be uncompetitive for practical applications. And the origin of such a dramatic deterioration was further discussed in the Mechanism section.

More surprisingly, the S-RP/C material is also sensitive to air and moisture. After that the S-RP/C were stored in ambient condition for one month, the XRD characteristic peaks of the RuP for S-RP/C vanished (Supplementary Fig. 17) and the bind energy of Ru 3p shift largely to reach the Ru 3p XPS peak of RuO_2 (Supplementary Fig. 18) along with the absence of the signal associating with phosphide in P 2p spectrum (Supplementary Fig. 18). These confirmed the excessively nanocrystallized RuP was completely oxidized. Interestingly, no phase change was detected by XRD for the L-RP/C under the same condition and even after six months of exposure to air (Supplementary Fig. 17), suggesting that large nanoparticles significantly improved chemical stability to oxygen and moisture. The HER performance of S-RP/C and L-RP/C after one month of storage in ambient air was evaluated. The HER activity of L-RP/C after one month resembled that of the fresh catalyst, while the performance of S-RP/C detoriarated drastically (Supplementary Fig. 19). Here, it is worth emphasizing that the large RuP nanoparticles not only enhanced catalytic activity, but also improved the chemical stability and catalytic durability, which is of significance for practical applications. Therefore, the L-RP/C becomes a promising catalyst with the remarkable activity and excellent stability.

The stabilities of the L-RP/C and Pt/C catalysts were further evaluated by chronopotentiometric (CP) measurements over extended periods in 1.0 M KOH, 0.5 M H_2SO_4 and 1.0 M PBS solution with a high catalyst loading of 2 mg cm^{-2} on the carbon cloth (Fig. 4b). In these tests, the L-RP/C displayed a nearly unchanged operating overpotential over a 200 h-testing period. In sharp contrast, the Pt/C underwent a rapid

degradation during the 100 h CP test. This indicates that L-RP/C possesses the greater potential than Pt/C for practical HER application.

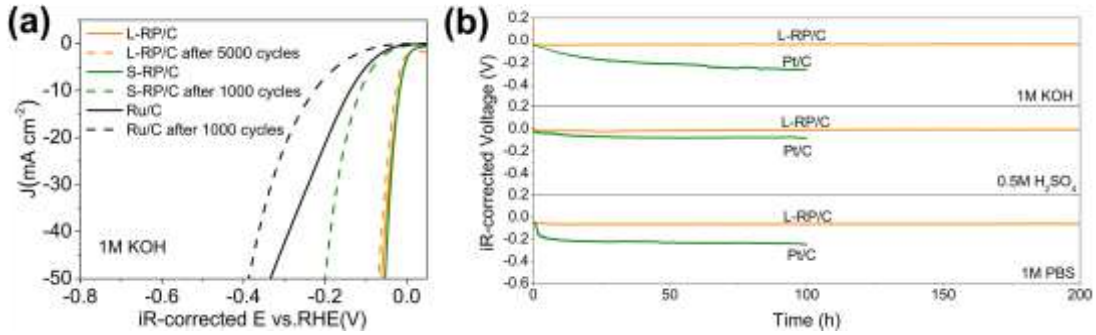

Figure 4 HER stability of different catalysts. (a) HER polarization curves of L-RP/C, S-RP/C, and Ru/C catalysts initially and after 5000 cycles and 1000 cycles, respectively, in 1 M KOH. (b) Chronopotentiometry curves of L-RP/C and Pt/C catalysts at a constant cathodic current density of -10 mA cm^{-2} in all pH solutions.

DFT Calculations

Based on above results, it is clear that RuP/C catalysts perform much better in activity than Ru/C, and Mayrhofer's group[23] has reported that metallic Ru is more active than RuO_2 for HER in identical experimental conditions. Actually, the formation of metal phosphides is one important way to improve the catalytic activity of metals for HER. For example, transition-metal phosphides (TMPs), including CoP[14, 30], NiP[28, 34], FeP[35], CoNiP[36, 37], CoFeP[38] and MoP[39, 40], have heavily emerged as the desirable HER electrocatalysts for their outstanding activity and low cost. Sun's group developed myriad of TMPs nanowires, nanosheets, or nanoarrays grown on different substrates via phosphorization of the corresponding precursor[41-44], as the high-performance catalysts towards HER. Schaak et al. successively proposed monodispersed Ni_2P and CoP nanoparticles as electrocatalysts for HER under strongly acidic conditions[28, 30]. The higher activity of metal phosphides as compared to their metallic counterparts is believed as a result from the more electronegativity of P atoms than the metals which can grab electron from metal atoms to modify the electronic structure of metal catalysts and act as well as a proton carrier[31].

To understand the superior performance of RuP as electrocatalysts for HER, the density functional theory (DFT) calculations were conducted as implemented in the Amsterdam Density Functional (ADF) package (version 2017)[45, 46]. The detailed calculation information could be obtained in the Supplementary Note 2. Firstly, it is well-known that the value of ΔG_{H^*} (* denotes an adsorption site) is considered as a key descriptor in theoretical prediction of the HER activity of an electrocatalyst [9, 47, 48]. An optimum HER electrocatalyst is suggested to be with a $|\Delta G_{H^*}|$ value approaching to 0, which affords a faster proton/electron transfer kinetics[9, 47, 48]. Therefore, the ΔG_{H^*} of RuP and Ru were calculated to predict the HER performance.

Various initial adsorption sites of H atom on the modeled surfaces were taken into account as shown in Fig. 5. For Ru (001) surface, we studied three H adsorption sites, i.e. the ruthenium atom top (T), the center (C) and the side of the triangle (S) formed by three Ru atoms (Fig. 5a). Note that, H atom at the T and S sites both rearranged to the C site after geometry optimization. Therefore, only the ΔG_{H^*} at the C site was calculated. For RuP (011) surface, the P_{3c} atom top (P_{3c}-T), the P_{4c} atom top (P_{4c}-T), the Ru_{6c} atom top (Ru_{6c}-T), the Ru_{5c}-T and the hollow (H) sites were investigated (Fig. 5b). Notably, after geometry optimization, hydrogen atom at the H site transferred to the Ru_{6c}-T site, and hydrogen atom at the P_{4c}-T site relocated to the Ru_{5c}-T site. Thus, the ΔG_{H^*} at the Ru_{6c}-T, Ru_{5c}-T and P_{3c}-T sites were computed. For RuP (112) surface, there are two types of Ru_{6c} atoms. Therefore, two Ru_{6c}-T sites (Ru_{6c}-1-T, Ru_{6c}-2-T, respectively) and the sites between each type of Ru_{6c} atoms (Ru_{6c}-1-M, Ru_{6c}-2-M, respectively.) were taken into account. The P_{3c}-T site was included as well (Fig. 5c).

The computed H adsorption energies (ΔE_{ads}) and ΔG_{H^*} are listed in Supplementary Table 3. The ΔE_{ads} of H at the P_{3c}-T site of RuP (011) surface, at the P_{3c}-T and Ru_{6c}-1-M sites of RuP (112) surface are positive. This implies that the H atom cannot adsorb at these sites. As illustrated in Fig. 5d, the Ru_{6c}-T site of RuP (011) surface shows the smallest $|\Delta G_{H^*}|$ value (0.002 eV) among three modeled surfaces and it is slightly smaller than that of RuP (112) Ru_{6c}-1-T site (0.086 eV), both of which are much smaller than the $|\Delta G_{H^*}|$ at the C site of Ru (001) (0.262 eV). Therefore, from the thermodynamic point of view, the hydrogen evolution activity of three surfaces is ordered as RuP (011) > RuP (112) > Ru (001), indicating that this RuP material should possess the superior catalytic activity for the HER.

In addition, the electric conductivities of RuP and Ru were evaluated by computing band gaps of these samples. The computed band gap of Ru (001) is 0 eV, indicating the metallic character. The RuP (011) surface has a band gap of 0.4 eV, which is between that of the metal and the semiconductor. The band gap of the RuP (112) surface is 0.06 eV, implying that the RuP (112) surface is more metallic than the RuP (011) surface. All in all, the computed zero or small band gaps of the current models reveal that these surfaces have sufficient electric conductivity to serve as the catalytic electrode.

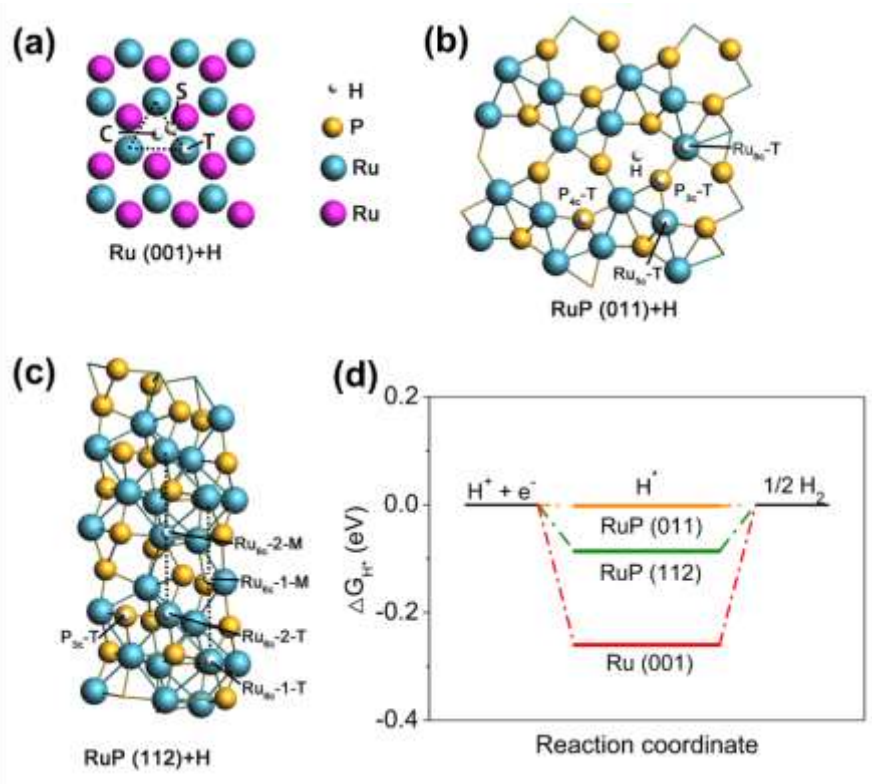

Figure 5 The initial adsorption sites of H atom on the modeled surfaces from the top view and HER-free energy diagram. (a) Ru (001) surface. The triangle formed by three Ru atoms of the first atomic layer is denoted using dotted lines. The Ru atoms from top to bottom layers are represented by cyan, magenta and green balls, respectively (The third atomic layer overlaps with the first one.). (b) RuP (011) surface. The P atoms are represented by orange balls. (c) RuP (112) surface. (d) Calculated HER-free energy diagram (ΔG_{H^*}) at the equilibrium potential for Ru and RuP.

Mechanism discussion

The above experiments revealed the unprecedented good HER intrinsic activity of RuP catalyst, which prompted us to probe the HER-enhanced mechanism. As is well-known, the ability of proton transfer has a significant impact on the HER performance, and a catalyst with phosphorus modification can enhance the interfacial proton transfer, as revealed by Yang *et al*[49]. Therefore, the RuP exhibited a superior HER activity than the metallic Ru sample. As depicted in Fig. 6a &b, the HER activity of the L-RP/C hybrid is strongly dependent on the pH value, suggesting the proton-transfer as a pivotal rate-determining step[49]. Moreover, DFT calculations, where the ΔG_{H^*} of RuP is close to 0 eV, further implied the faster proton/electron transfer kinetics.

Observing the significant differences of the stability and intrinsic catalytic activity between the S-RP/C and L-RP/C catalysts, we propose that the dissolution of phosphorus for S-RP/C caused the dramatic deterioration of the HER activity during the durability tests. The P 2p spectrum after the stability test confirmed the considerable change in content of the phosphorus element in S-RP/C (Fig. 6c). Although the smaller nanoparticles expose more active sites relative to the larger one, the mutability of S-RP

particles in air environment and under operation conditions makes that the intrinsic catalytic activity of S-RP/C is much lower than that of L-RP/C. Besides, the S-RP particles with the size of 1-3 nm exhibit the higher surface energy, thus the more active P-O is dissolved more easily. In contrast, the large particles with the lower surface energy are more stable and the ultrathin surface P-O layers are still retained on the L-RP after stability test (Fig. 6f), which is responsible for the improved proton transfer. Additionally, as observed from Ru 3p spectrum and HRTEM images of the L-RP/C and S-RP/C samples after the stability tests in Fig. 6d-h, the two samples both showed the phase structure of RuP, but the amount of RuP nanoparticles on the surface of S-RP/C after the stability test was distinctly decreased, in agreement with the XPS results, which is due to the dissolution of RuP (Supplementary Table 4). For O 1s spectra of L-RP/C and S-RP/C after stability tests (Supplementary Fig. 20), there is a peak appeared after the stability test within the range of 535-536.5 eV for RuP, corresponding to the contribution of the chemisorbed oxygen like H_2O, OH^{-}[50]. The high hygroscopicity is attributed to the P species on the surface of RuP. At intial tests, both L-RP/C and S-RP/C samples showed the excellent HER activity and their O 1s spectrum in the range of 535-536.5 eV are markedly present (Supplementary Fig. 21). As a comparison, the peak from 535-536.5 eV was extremely weak for S-RP/C after the tests (Supplementary Fig. 20), indicating the dissolution of phosphorus from S-RP/C.

To gain further insights on the instability of S-RP/C deriving from the dissolution of phosphorus, the pH-dependent HER activities of L-RP/C and S-RP/C were compared between the initial tests and the tests after 500 cycles. As shown in Fig. 6a&b, the pH-dependent HER activity of L-RP/C for the initial testing is nearly overlapped with that of the L-RP/C after 500-cycles testing, whereas the performance of S-RP/C was decreased through the 500-cycles testing and had a weakened dependence on pH, so the interfacial proton transfer of S-RP/C was lowered. Aware of these, it demonstrates that the dissolution of phosphorus whittles the ability of proton transfer and results in the unsteadiness of S-RP/C during the operation.

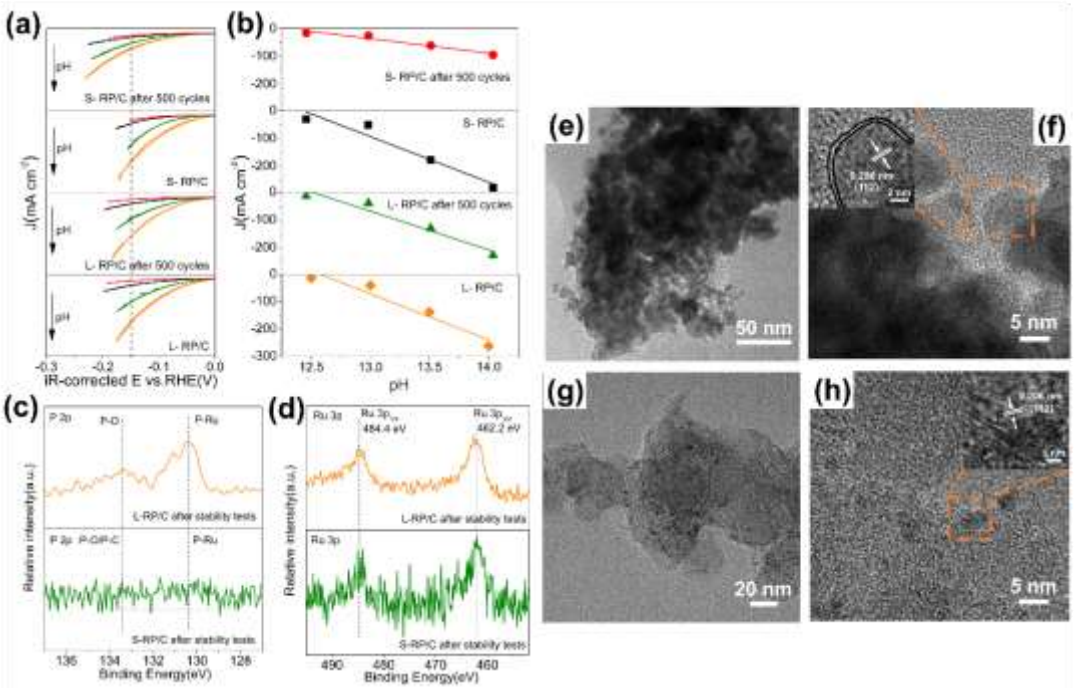

Figure 6 pH dependence of the HER activity and structure characterization after stability tests. (a) HER CV curves of L-RP/C and S-RP/C catalysts initially and after 500 cycles in KOH solutions with pH increasing from 12.5 to 14. (b) Comparison of the current densities measured at -0.15 V vs RHE at different pH values. (c, d) High-resolution P 2p (c) and Ru 3p (d) XPS spectra of the L-RP/C and S-RP/C samples initially and after stability tests in 1 M KOH. (e-h) HRTEM images of the L-RP/C (e, f) and S-RP/C (g, h) samples after stability tests in 1 M KOH.

Overall water splitting by L-RP/C and L-RO/C

A two-electrode electrolytic cell with an alkaline electrolyzer was constructed to go a step closer to real applications using L-RP/C loaded on Ni foam as the cathode catalyst for HER and L-RO/C (the mixture of RuO_2 and conductive carbon, the synthetic procedure of which could be found in **Catalysts synthesis**.) loaded on Ni foam as the anode catalyst for OER (the OER activity of L-RO/C is compared with the commercial RuO_2/C in Supplementary Fig. 22). At an applied current density of 10 mA cm^{-2}, water electrolysis occurred at a potential difference of 1.49 V between the anode and the cathode. Notably, this was rarely reported to achieve a voltage of less than 1.5 V at a current density of 10 mA cm^{-2} for water electrolysis. Such overall water splitting could be powered by a single-cell AAA battery with a nominal voltage of ~1.5 V (Inset of Fig. 5d and Supplementary Movie 1). As a control, two-electrode electrolyzers comprised of Ni foam//Ni foam and Pt/C//RuO_2 were also configured as references. It is highly exciting to note that the water-splitting performance of L-RP/C//L-RO/C show more remarkable activity than that of the benchmark Pt/C//RuO_2 couple (Fig. 7a) and was comparable to that of other water splitting processes carried out using state-of-the-art catalysts (Supplementary Table 5). Besides, the L-RP/C//L-RO/C electrodes maintain strong stability over 50 h water splitting testing as compared to the benchmark

Pt/C//IrO_2 couple (Fig. 7b). Hence, the L-RP/C//L-RO/C couple holds great promise for practical alkaline water electrolysis application.

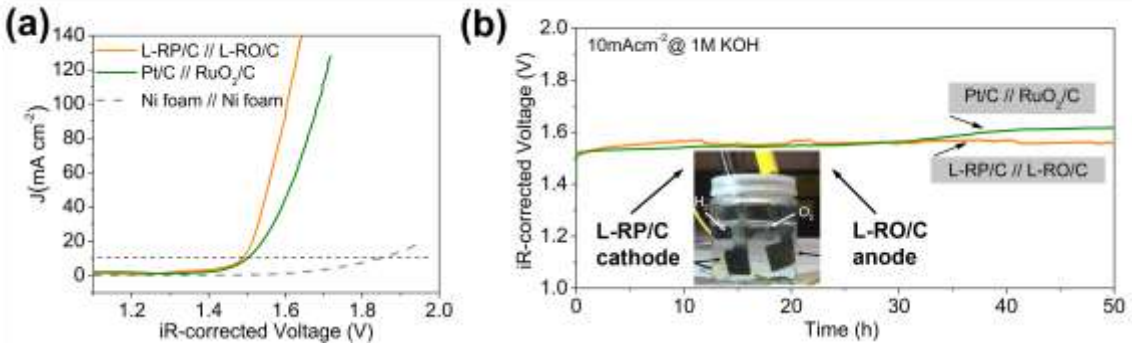

Figure 7 Overall water splitting with L-RP/C as the cathode. (a) Polarization curves of L-RP/C(−)//L-RO/C(+), Pt/C(−)//RuO_2(+), and bare Ni foam//Ni foam for overall water splitting in 1 M KOH solution with the loading of 8 mg cm^{-2}. Scan rate, 5 mV s^{-1}. (b) Chronopotentiometry curves of water electrolysis using L-RP/C(−)//L-RO/C(+) and Pt/C(−)//RuO_2(+) couples at a constant current density of 10 mA cm^{-2} in 1 M KOH. Inset: A representative photograph of water-splitting device powered by an AAA battery with a nominal voltage of 1.5V.

In conclusion, RuP, as an upcoming star for HER, displayed the unprecedentedly high HER activity and the enhanced HER stability relative to the metallic Ru. The theoretical studies also validated the result. Moreover, the sizes of RuP particles were controlled and the bigger one makes surprisingly better. Due to the coarse type nature, the L-RP/C sample has 50 folds of improvement in intrinsic catalytic activity of RuP for HER as compared to the S-RP/C sample. Moreover, the catalytic durability and chemical stability split the gap between L-RP/C and S-RP/C, making L-RP/C more promising as a HER catalyst. The L-RP/C exhibits the low η_{10} (18 mV in 1 M KOH solution; 19.0 mV in 0.5 M H_2SO_4 solution; 80 mV in 1 M PBS solution) and high j_0 (3.07 mA cm^{-2} in 1 M KOH solution; 3.22 mA cm^{-2} in 0.5 M H_2SO_4 solution; 0.58 mA cm^{-2} in 1 M PBS solution), as well as superior stability for 200 h in all pH solution, exceeding almost all the documented electrocatalysts including the benchmark 20% Pt/C catalysts, particularly in basic media. More importantly, L-RP/C with the low content of Ru provide it a huge economical advantage in price over commercial Pt/C catalysts and the L-RP/C was conveniently and efficiently prepared, which benefit to industrial production. As a result, this study facilitates the development of newly efficient HER catalysts to thoroughly replace Pt/C.

Methods

Catalysts synthesis

Synthesis of L-RP/C and Ru/C

The L-RP was first prepared through a one-step low-temperature phosphorization

method. Specifically, the commercial ruthenium chloride ($RuCl_3$) and NaH_2PO_2 were put at two separate positions in a porcelain-boat with 1.0 g of NaH_2PO_2 at the upstream side of the furnace. Afterwards, they undergone heat treatment at 400 °C for 1 h with a heating rate of 2 °C min^{-1} in a static Ar atmosphere and then naturally cooled down to ambient temperature to obtain coarse-type RuP particles (L-RP). The metal Ru was also synthesized following the identical heating procedure at H_2/Ar, with the absence of NaH_2PO_2. Eventually, this sample was mixed with conductive carbon in appropriate proportions to produce the resultant catalysts.

Synthesis of S-RP/C

Briefly, 40 mg ruthenium chloride ($RuCl_3$) were dissolved in a 20 ml ethanol system under agitated stirring at room temperature to get an absolutely transparent solution. Subsequently, a certain amount of conductive carbon was impregnated with the above solution. After vigorous stirring at 323 K for 12 h, a black solid precursor was collected and finally was phosphidated by the similar process to those described above. The resulting product was denoted as S-RP/C.

Synthesis of L-RO/C

The L-RO were prepared by using the identical heating procedure with L-RP at air atmosphere with the absence of NaH_2PO_2. Then, the sample was mixed with conductive carbon in appropriate proportions to obtain the L-RO/C sample (The RuO_2 content in the L-RO/C product is about 20 wt%).

Characterizations

Powder X-ray powder diffraction (XRD) for structure identification was carried out on a Rigaku Smartlab diffractometer using filtered Cu-Kα radiation (λ =1.5418Å) with 2θ range of 10-90° and operating at a tube voltage of 40 kV and current of 40 mA. The morphologies of the samples were characterized by a field-emission scanning electron microscope (FE-SEM, HITACHI-S4800) and a transmission electron microscope (TEM, FEI Tecnai G2T20) operating at 200 kV. And the corresponding Scanning TEM (STEM)-EDX line scan and element mapping were taken on an FEI Tecnai G2 F30 STWIN field-emission transmission electron microscope equipped with an EDX analyzer at 200 kV. The specific surface areas and pore size distributions were obtained by the measurement of the N_2-adsorption-desorption on a BELSOR-MAX instrument using the Brunauer-Emmett-Teller (BET) and Barrett-Joyner-Halenda (BJH) methods. Thermogravimetric (TG) analysis was performed on a thermobalance (STA 449 *F3* Jupiter®, NETZSCH) under air flow to determine the metal content of the product. The chemical compositions and surface element states were also probed by X-ray photoelectron spectroscopy (XPS) on a PHI5000 VersaProbe spectrometer equipped with an Al-Kα X-ray source and the datas were fitted by the public software package

XPSPEAK.

Electrode preparation and electrochemical characterization

All electrochemical performance was measured under ambient temperature in a standard three-electrode electrochemical cell with the glassy carbon/ carbon cloth (stability testing-chronopotentiometric (CP) measurements) as the working electrode substrate, a graphite rod as the counter electrode and Ag|AgCl (3.5 M KCl) as the reference electrode by using a CHI 760E Bipotentiostat. In order to provide a wide electrochemical operating environment with different pHs (0-14), 1 M KOH, 0.5M H_2SO_4 and 1 M PBS solution were used as electrolytes, respectively. 10 mg of each catalyst sample and 50 μL of 5 wt % Nafion solution were dispersed in 0.5 mL of ethanol by sonication for at least 1 hour to form the homogeneous working electrode ink. Then, a 5 μL of ink aliquot was transferred onto glassy carbon substrate with 5 mm diameter, leading to an approximate catalyst loading of 0.464 mg cm^{-2}. When the carbon cloth was used for stability testing, the catalyst loading is 2 mg cm^{-2}.

The electrolyte was continuously bubbled with Ar for approximately 30 min prior to HER measurements and then maintained under Ar atmosphere till the end of test. Hundreds of potential cycles were first carried out to make pretreatment at different potential regions versus Ag|AgCl for HER tests in all pH values. Subsequently, HER polarization curves obtained from linear sweep voltammetry (LSV) were recorded on a rotating disk electrode (RDE) at a scan rate of 5 mV s^{-1} from different potential regions versus Ag|AgCl in diverse pH media with constant rotation speeds of 1600rpm get rid of the bubbles. All potentials were referenced to a reversible hydrogen electrode (RHE) after iR compensation: $E_{RHE} = E_{Ag/AgCl} + 0.197 + 0.059 \times pH$. The polarization curves were replotted as overpotential (η) versus the logarithm of current density (log |j|) to obtain Tafel plots. And electrochemical impedance spectra (EIS) measurements were carried out over a frequency range from 100 kHz to 0.1 Hz under the influence of an AC voltage of 5 mV. The electrochemical double-layer capacitance (EDLCs), Cdl, was obtained from cyclic voltammetry curves (CVs) recorded in a potential range with no faradic current at different rates from 20 to 120 mV s^{-1}. The turnover frequency (TOF) of various electrocatalysts were calculated based on the previously reported method. Accelerated stability tests of the catalysts were conducted by continuous potential cycling at a sweep rate of 100 mV s^{-1} for a given number of cycles. The long-term chronopotentiometric (CP) measurements were studied at a constant cathodic current density of 10 mA cm^{-2} for 200 h. The overall water electrolysis measurement was performed in a home-made two electrode system with catalysts coated on Ni foam (mass loading: 5 mg cm^{-2}). The polarization curves were obtained with the scan rate of 5 mV s^{-1} and further *iR*-corrected.

1. Chu, S. & Majumda,r A. Opportunities and challenges for a sustainable energy future. *Nature* **488**, 294-303 (2012).

2. Subbaraman, R. et al Enhancing Hydrogen Evolution Activity in Water Splitting by Tailoring Li+-Ni(OH)$_2$-Pt Interfaces. *Science* **334**, 1256-1260 (2011).

3. Shi, Y. & Zhang, B. Recent advances in transition metal phosphide nanomaterials: synthesis and applications in hydrogen evolution reaction. *Chem. Soc. Rev.* **45**, 1529-1541 (2016).

4. Turner, J. A. Sustainable hydrogen production. *Science* **305**, 972-974 (2004).

5. Edwards, P. P., Kuznetsov, V. L., David, W. I. F. & Brandon, N. P. Hydrogen and fuel cells: Towards a sustainable energy future. *Energ. Policy* **36**, 4356-4362 (2008).

6. Jiao, Y., Zheng, Y., Davey, K. & Qiao, S. Z. Activity origin and catalyst design principles for electrocatalytic hydrogen evolution on heteroatom-doped graphene. *Nat. Energy* **1**, 16130 (2016).

7. Halter, D. P., Heinemann, F. W., Bachmann, J. & Meyer, K. Uranium-mediated electrocatalytic dihydrogen production from water. *Nature* **530**, 317-321 (2016).

8. Xu, X. *et al.* A Perovskite Electrocatalyst for Efficient Hydrogen Evolution Reaction. *Adv. Mater.* **28**, 6442-6448 (2016).

9. Su, J., Yang, Y., Xia, G., Chen, J. & Jiang, P. *et al* Ruthenium-cobalt nanoalloys encapsulated in nitrogen-doped graphene as active electrocatalysts for producing hydrogen in alkaline media. *Nat. commun.* **8**, 14969 (2017).

10. Gao, M. R. *et al.* An efficient molybdenum disulfide/cobalt diselenide hybrid catalyst for electrochemical hydrogen generation. *Nat. commun.* **6**, 5982 (2015).

11. Yin, J. *et al.* Ni-C-N Nanosheets as Catalyst for Hydrogen Evolution Reaction. *J. Am. Chem. Soc.* **138**, 14546-14549 (2016).

12. Zhu, Y. *et al.* A Perovskite Nanorod as Bifunctional Electrocatalyst for Overall Water Splitting. *Adv. Energy Mater.* **7**, 1602122 (2017).

13. Rheinlaender, P. J., Herranz, J., Durst, J. & Gasteiger, H. A. Kinetics of the Hydrogen Oxidation/Evolution Reaction on Polycrystalline Platinum in Alkaline Electrolyte Reaction Order with Respect to Hydrogen Pressure. *J. Electrochem. Soc.* **161**, F1448-F1457 (2014).

14. Xue, Z. H. *et al.* Janus Co/CoP Nanoparticles as Efficient Mott-Schottky Electrocatalysts for Overall Water Splitting in Wide pH Range. *Adv. Energy Mater.* **7**, 1602355 (2017).

15. Zheng, Y. *et al.* High Electrocatalytic Hydrogen Evolution Activity of an Anomalous Ruthenium Catalyst. *J. Am. Chem. Soc.* **138**, 16174-16181 (2016).

16. Chen, P. *et al.* Metallic Co_4N Porous Nanowire Arrays Activated by Surface Oxidation as Electrocatalysts for the Oxygen Evolution Reaction. *Angew. Chem. Int. Edit.* **54**, 14710-14714 (2015).

17. Durst, J. *et al.* New insights into the electrochemical hydrogen oxidation and evolution reaction mechanism. *Energ. & Environ. Sci.* **7**, 2255-2260 (2014).

18. Mahmood, J. *et al.* An efficient and pH-universal ruthenium-based catalyst for the hydrogen evolution reaction. *Nat. nanotechnol.* **12**, 441-446 (2017).

19. Masa, J. *et al.* Low Overpotential Water Splitting Using Cobalt–Cobalt Phosphide Nanoparticles Supported on Nickel Foam. *ACS Energy Lett.* **1**, 1192-1198 (2016).

20. Liang, H. W. *et al.* Molecular metal-Nx centres in porous carbon for electrocatalytic hydrogen evolution. *Nat. commun.* **6**, 7992 (2015).

21. Kong, X. *et al.* Free-Standing Two-Dimensional Ru Nanosheets with High Activity toward Water Splitting. *ACS Catal.* **6**, 1487-1492 (2016).

22. Bhowmik, T., Kundu, M. K. & Barman, S. Growth of One-Dimensional RuO_2 Nanowires on g-Carbon Nitride: An Active and Stable Bifunctional Electrocatalyst for Hydrogen and Oxygen Evolution Reactions at All pH Values. *ACS Appl. Mater. Inte.* **8**, 28678-28688 (2016).

23. Cherevko, S. *et al.* Oxygen and hydrogen evolution reactions on Ru, RuO_2, Ir, and IrO_2 thin film electrodes in acidic and alkaline electrolytes: A comparative study on activity and stability. *Catal. Today* **262**, 170-180 (2016).

24. Teller, H., Krichevski, O., Gur, M., Gedanken, A. & Schechter, A. Ruthenium phosphide synthesis and electroactivity toward oxygen reduction in acid solutions. *ACS Catal.* **5**, 4260-4267 (2015).

25. Liang, H. *et al.* Amorphous NiFe-OH/NiFeP Electrocatalyst Fabricated at Low Temperature for Water Oxidation Applications. *ACS Energy Lett.* **2**, 1035-1042 (2017).

26. Yang, H., Zhang, Y. Hu, F. & Wang, Q. Urchin-like CoP Nanocrystals as Hydrogen Evolution Reaction and Oxygen Reduction Reaction Dual-Electrocatalyst with Superior Stability. *Nano Lett.* **15**, 7616-7620 (2015).

27. Chang, J. *et al.* Surface Oxidized Cobalt-Phosphide Nanorods As an Advanced Oxygen Evolution Catalyst in Alkaline Solution. *ACS Catal.* **5**, 6874-6878 (2015).

28. Popczun, E. J. *et al.* Nanostructured nickel phosphide as an electrocatalyst for the hydrogen evolution reaction. *J. Am. Chem. Soc.* **135**, 9267-9270 (2013).

29. Laursen, A. B. *et al.* Nanocrystalline Ni_5P_4: a hydrogen evolution electrocatalyst of exceptional efficiency in both alkaline and acidic media. *Energ. & Environ. Sci.* **8**, 1027-1034 (2015).

30. Popczun, E. J., Read, C. G., Roske, C. W., Lewis, N. S. & Schaak, R. E. Highly active electrocatalysis of the hydrogen evolution reaction by cobalt phosphide nanoparticles. *Angew. Chem. Int. Edit.* **53**, 5427-5430 (2014).

31. Tian, J., Liu, Q., Asiri, A. M. & Sun, X. Self-supported nanoporous cobalt phosphide nanowire arrays: an efficient 3D hydrogen-evolving cathode over the wide range of pH 0-14. *J. Am. Chem. Soc.* **136**, 7587-7590 (2014).

32. Ma, L., Ting, L. R. L., Molinari, V., Giordano, C. & Yeo, B. S. Efficient hydrogen evolution reaction catalyzed by molybdenum carbide and molybdenum nitride nanocatalysts synthesized via the urea glass route. *J. Mater. Chem. A* **3**, 8361-8368 (2015).

33. Fei, H. et al. Atomic cobalt on nitrogen-doped graphene for hydrogen generation. *Nat. Commun.* **6**, 8668 (2015).

34. Chen, G. F. *et al.* Efficient and Stable Bifunctional Electrocatalysts Ni/Ni_xM_y (M = P, S) for Overall Water Splitting. *Adv. Funct. Mater.* **26**, 3314-3323 (2016).

35. Chung, D. Y. *et al.* Large-Scale Synthesis of Carbon-Shell-Coated FeP Nanoparticles for Robust Hydrogen Evolution Reaction Electrocatalyst. *J. Am. Chem. Soc.* **139**, 6669-6674 (2017).

36. Li, J. *et al.* Mechanistic Insights on Ternary Ni2−xCoxP for Hydrogen Evolution and Their Hybrids with Graphene as Highly Efficient and Robust Catalysts for Overall Water Splitting. *Advanced Functional Materials* **26**, 6785-6796 (2016).

37. Pan, Y. *et al.* Cobalt nickel phosphide nanoparticles decorated carbon nanotubes as advanced hybrid catalysts for hydrogen evolution. *J Mater. Chem. A* **4**, 14675-14686 (2016).

38. Mendoza-Garcia, A., Su, D. & Sun, S. Sea urchin-like cobalt-iron phosphide as an active catalyst for oxygen evolution reaction. *Nanoscale* **8**, 3244-3247 (2016).

39. Xiao, P. *et al.* Molybdenum phosphide as an efficient electrocatalyst for the hydrogen evolution reaction. *Energ. & Environ. Sci.* **7**, 2624-2629 (2014).

40. Chen, X. *et al* Molybdenum phosphide: a new highly efficient catalyst for the electrochemical hydrogen evolution reaction. *Chem. Commun.* **50**, 11683-11685 (2014).

41. Tang, C. *et al.* Ternary $Fe_xCo_{1-x}P$ Nanowire Array as a Robust Hydrogen Evolution Reaction Electrocatalyst with Pt-like Activity: Experimental and Theoretical Insight. *Nano Lett.* **16**, 6617-6621 (2016).

42. Tang, C. *et al.* Fe-Doped CoP Nanoarray: A Monolithic Multifunctional Catalyst for Highly Efficient Hydrogen Generation. *Adv. Mater.* **29**, 1602441 (2017).

43. Zhang, R. *et al.* Al-Doped CoP nanoarray: a durable water-splitting electrocatalyst with superhigh activity. *Nanoscale* **9**, 4793-4800 (2017).

44. Zhang, Y. *et al.* A Mn-doped Ni_2P nanosheet array: an efficient and durable hydrogen evolution reaction electrocatalyst in alkaline media. *Chem. Commun.* DOI: 10.1039/C7CC06278H (2017).

45. Velde, G. T. & Baerends, E. J. Precise density-functional method for periodic structures. *Phys. Rev. B* **44**, 7888-7903 (1991).

46. Philipsen, P. H. T. *et al.* BAND2017, SCM, Theoretical Chemistry, Vrije Universiteit, Amsterdam, The Netherlands, http://www.scm.com.

47. Duan, H. *et al.* High-Performance Rh_2P Electrocatalyst for Efficient Water Splitting. *J. Am. Chem. Soc.* **139**, 5494-5502 (2017).

48. Yang, F., Chen, Y., Cheng, G., Chen, S. & Luo, W. Ultrathin Nitrogen-Doped Carbon Coated with CoP for Efficient Hydrogen Evolution. *ACS Catal.* **7**, 3824-3831 (2017).

49. Yang, C. *et al.* Phosphate Ion Functionalization of Perovskite Surfaces for Enhanced Oxygen Evolution Reaction. *J. Phys. Chem. Lett.* **8**, 3466-3472 (2017).

50. Desimoni, E., Casella, G. L., Morone, A. & Salvi, A. M. XPS Determination of Oxygen-containing Functional Groups on Carbon-fibre Surfaces and the Cleaning of These Surfaces. *Surf. Interface Anal.* **15**, 627-634 (1990).